Flapping dynamics and wing flexibility enhance odor detection in blue bottle flies

Bioinspiration & Biomimetics

PAPER

Flapping dynamics and wing flexibility enhance odor detection in blue bottle flies

Naeem Haider[1], Zhipeng Lou[1], Shih-Jung Hsu[2], Bo Cheng[2] and Chengyu Li[1,*]

[1] Department of Mechanical and Aerospace Engineering, Case Western Reserve University, Cleveland, OH 44106, United States of America
[2] Department of Mechanical Engineering, Pennsylvania State University, University Park, PA 16802, United States of America
* Author to whom any correspondence should be addressed.

E-mail: cxl1692@case.edu

Keywords: flapping flight, unsteady aerodynamics, wing-induced flow, olfactory sensation, odor-guided navigation

OPEN ACCESS

RECEIVED
2 January 2025

REVISED
7 February 2025

ACCEPTED FOR PUBLICATION
19 February 2025

PUBLISHED
11 March 2025

Abstract

One of the most ancient and evolutionarily conserved behaviors in the animal kingdom involves utilizing wind-borne odor plumes to track essential elements such as food, mates, and predators. Insects, particularly flies, demonstrate a remarkable proficiency in this behavior, efficiently processing complex odor information encompassing concentrations, direction, and speed through their olfactory system, thereby facilitating effective odor-guided navigation. Recent years have witnessed substantial research explaining the impact of wing flexibility and kinematics on the aerodynamics and flow field physics governing the flight of insects. However, the relationship between the flow field and olfactory functions remains largely unexplored, presenting an attractive frontier with numerous intriguing questions. One such question pertains to whether flies intentionally manipulate the flow field around their antennae using their wing structure and kinematics to augment their olfactory capabilities. To address this question, we first reconstructed the wing kinematics based on high-speed video recordings of wing surface deformation. Subsequently, we simulated the unsteady flow field and odorant transport during the forward flight of blue bottle flies (*Calliphora vomitoria*) by solving the Navier–Stokes equations and odorant advection–diffusion equations using an in-house computational fluid dynamics solver. Our simulation results demonstrated that flexible wings generated greater cycle-averaged aerodynamic forces compared to purely rigid flapping wings, underscoring the aerodynamic advantages of wing flexibility. Additionally, flexible wings produced 25% greater odor intensity, enhancing the insect's ability to detect and interpret olfactory cues. This study not only advances our understanding of the intricate interplay between wing motion, aerodynamics, and olfactory capabilities in flying insects but also raises intriguing questions about the intentional modulation of flow fields for sensory purposes in other behaviors.

1. Introduction

Insects exhibit a remarkable ability to navigate their environments using sophisticated sensory systems [1, 2]. One of the most crucial sensory modalities is olfaction, which allows insects to detect and interpret chemical signals in their surroundings. This capability is vital for a variety of behaviors, including foraging, mating, and avoiding predators. Insects rely on their antennae, specialized sensory organs that play a critical role in detecting odors. Additionally, the antennae are mechanosensitive, capable of detecting changes in airflow, which provide critical feedback for stabilizing flight and navigating wind-borne odor plumes [3–6]. Studies have shown that antennae play a complementary role to vision, with mechanosensory feedback enabling fast responses to airflow changes, while vision provides delayed but essential information about surroundings, including ground-speed estimation [7, 8]. This integration of sensory modalities enables insects to adapt to complex and dynamic environments with remarkable efficiency.

During flapping flight, the unsteady aerodynamics of insect wings are a critical aspect of their flight mechanics, which directly impacts their ability to utilize olfactory cues effectively [9]. Insect flight is characterized by dynamic wing movements that generate lift and manage drag [10–13]. In forward flight, the lift force is predominantly produced during the downstroke, while drag is primarily managed during the upstroke [10–13]. Computational fluid dynamics (CFD) simulations have provided insights into the distribution of aerodynamic forces, revealing that most of the lift is generated around the leading edge of the wing, while power consumption is concentrated around the wingtip [10–13]. These aerodynamic features not only support stable flight but also facilitate the insect's ability to follow wind-borne odor plumes by maintaining proper positioning relative to the airflow. The integration of this aerodynamic feedback with olfactory sensory input is essential for efficient navigation in complex environments. Recent studies, such as those by Fuller *et al* and Patel *et al* have shown that the coordination of flight dynamics and olfactory processing enables insects to rapidly adjust their flight path in response to changes in wind and odor gradients [7, 14]. These findings demonstrate that the coordination between aerodynamic forces, flight dynamics, and olfactory sensory input allows insects to track odor plumes and navigate through varying environmental conditions more efficiently. This synergy between the aerodynamic and sensory systems is key to optimizing both flight and olfactory behaviors, ensuring that insects can quickly respond to changes in their surroundings.

While studies suggest that the antennae response in flying insects is tuned to the periodicity of wing beats [15], this does not imply that wing beats directly function as a 'sniffing' mechanism. Instead, the periodicity of the wing beats may influence the timing of olfactory processing, as the insect's sensory systems, including the antennae, are tuned to environmental cues that fluctuate in sync with flight dynamics. The flapping motion of insect wings generates oscillations in the surrounding air, modulating the concentration of odor molecules near the antennae [5]. Research has demonstrated that wing motion increases the concentration of odors around the antenna and introduces pulses in odor plumes, which helps insects maintain sensitivity and effectively track odors [16, 17]. Studies such as those by Tripathy *et al* [18] have shown that these oscillations prevent sensory adaptation, allowing insects to follow odor plumes more accurately. However, Tripathy *et al* primarily focusses on the antennal and antennal lobe responses to odorants pulsed at frequencies matching the natural wingbeat frequency. Their study does not directly show that the movement of the wings enhances odor concentrations or generates pulses within the odor plumes. To support the broader idea of wing motion influencing odor concentration, Lou *et al,* conducted numerical simulations on monarch butterflies [6]. Their findings indicate that the interaction between wing flapping motion and the antennae significantly increases fluctuations in odor intensity along the antennae. In their simulations, the amplitude of these fluctuations was enhanced by up to 8.4 times due to the wing–antenna interaction, with wing-induced flow accounting for up to 88.10% of the odor fluctuation. This emphasizes the role of wing motion in enhancing odor concentration and olfactory performance during flight. Several Studies have investigated the interaction between odor fluctuations and sensory efficiency during insect flight, highlighting how turbulent plumes and pulsed odor signals aid navigation [19–21]. These works emphasize that odor detection and tracking are facilitated by intermittent odor encounters, which prevent sensory adaptation and maintain high sensitivity. Although they do not explicitly claim that moth wings direct odor toward the antenna, they underline the role of fluctuating odor signals in enhancing navigational efficiency and the ability to locate odor sources in complex environments.

The role of wing motion in enhancing odor tracking has been explored across various insect species. Li *et al* [3] found that this wing motion increases the odor intensity around fruit fly antennae by approximately 1.8 times during forward flight. The studies highlight that insect wing motion plays a critical role in enhancing olfactory function by generating oscillations that increase odor concentration, create odor pulses, prevent sensory adaptation, and improve navigation within odor plumes. Cardé *et al* [5] investigated how insects detect odors in distant wind-borne plumes, while Menzel and Greggor [22] examined odor-guided navigation in honeybees, revealing their ability to follow odors over distances exceeding 300 m. Saxena *et al* [23] studied odor tracking in fruit flies and observed how they adjust speed and direction in response to odor plumes. Freas and Spetch [24] investigated various navigational strategies in insects, focusing on how they utilize different visual cues to navigate through complex odor environments. The spatial distribution of odor intensity along the antenna varies, with different regions exhibiting varying sensitivities to odor stimuli.

Beyond wing motion, the interaction between aerodynamic forces and olfactory performance is influenced by flight dynamics and environmental turbulence. During flight, insects encounter turbulent airflows that affect odor dispersion and detection. Research has shown that turbulence generated by wing flapping can either enhance or disrupt odor tracking, depending on the airflow conditions and the structure of the odor plume [25]. Lei *et al* [25], investigated how wing-induced turbulence influences the structure of odor plumes, affecting an insect's ability

to detect and respond to odors. Lei and Li [26] further demonstrated that the effectiveness of odor reception varies with flight speed. At lower reduced frequencies, wing motion interferes with odor transport, while at higher frequencies, it enhances sensitivity to odors. Additionally, passive wing pitching has been shown to direct odor plumes toward an insect's antennae, as observed in fruit flies [27]. Lionetti *et al* [28] studied how wind speed impacts the olfactory capabilities of hawkmoths, reporting that odor intensity near the antenna is 39% greater at lower speeds (2 m s^{-1}) than at higher speeds (4 m s^{-1}).

Despite the advancements in understanding aerodynamic performance and olfactory navigation, there is a notable gap in research that integrates these aspects. While individual studies have explored insect flight dynamics and wing motion effects on olfaction, the interaction between these domains remains inadequately understood. Comprehensive research combining aerodynamic simulations with olfactory performance analyses is essential for elucidating the complex relationship between flight dynamics and odor detection. This study aims to address these gaps by investigating the blue bottle fly's wing motion and its impact on olfactory performance.

Flies are renowned for their exceptional flying capabilities, demonstrating proficiency across a wide range of speeds and executing highly agile maneuvers [29–31]. Extensive research has been conducted to understand the aerodynamics of flies, including studies by Engles *et al* who measured aerodynamic efficiency across various fly types. Their research explored different vane structures and wing flexibility, as well as the effects of corrugation on aerodynamic performance [29–31]. Additionally, Hsu *et al* conducted a focused study on the blue bottle fly, employing a magnetically levitated (MAGLEV) flight mill to measure flight speed and wing kinematics. Their study involved observing the blue bottle fly at multiple speeds and calculating the corresponding wing kinematics for each velocity scenario [29–31].

By utilizing the MAGLEV flight mill to record the fly's flight, we reconstructed its wing, body, and kinematics and simulated them using an immersed boundary method (IBM) in our solver. An odor source was strategically placed in front of the fly during simulations to evaluate olfactory performance. This study aims to address several key research questions related to the interplay between wing motion and olfactory performance in blue bottle flies. First, it seeks to determine how wing motion affects olfactory performance by investigating the impact of wing-induced airflow on the fly's ability to detect odors. To achieve this, the research compares aerodynamic simulations across different wing motion scenarios. Second, the study explores the differences in olfactory performance between three distinct scenarios: one with natural wing motion (baseline case), one without wing motion (body-only case), and one with a rigid wing model. This comparison aims to quantify how the presence and dynamics of wing motion influence odor detection. By analyzing these simulations in various scenarios, the research seeks to understand the relationship between aerodynamic forces and the fly's ability to sense and navigate towards odors.

2. Methodology

2.1. Experimental setup and filming procedures

Blue bottle fly (*Calliphora Vomitoria*) flight was observed using a MAGLEV flight mill comprised of four main components which includes shaft, walls, magnets, and cameras. The mill consists of only one shaft with a damper which allows only horizontal motion. One inner and one outer wall which act as boundary. For high-speed video recording, three cameras are placed for the bottom side and top view. The flies were documented within a circular enclosure measuring (50 mm × 50 mm × 50 mm) using three cameras strategically placed at the top, side (via a circular hole in the outer wall), and bottom, as illustrated in figure 1. The resolution was set at 1280 ×1024 pixels with a frame rate of 4000–1 and a shutter rate of 8000–1. To illuminate the enclosure, three 100 W LED lights (MonoBright LED Bi-color 750, Genaray, Brooklyn, NY, USA) were employed. The fly was affixed to the damper on its dorsal thorax using UV cure glue (4305, Loctite Corp.), enabling attachment to the rotating shaft for forward flight. Various fly speeds were recorded, with a forward speed of 1.24 m s^{-1} selected for this study. Morphological parameters for the fly are detailed in table 1.

2.2. Reconstruction of blue bottle fly flight

The reconstruction of both the body and wings, incorporating surface deformation, employed Autodesk MAYA (Autodesk, San Raphael, CA, USA). Specifically, one wing beat cycle was meticulously selected for the extraction of wing kinematics, and the subsequent reconstruction focused solely on the left wing, with an identical process applied to the right wing. Noteworthy is the absence of any distinct body deformation or rotation throughout the reconstruction process. This particular cycle was chosen because the insect's top, bottom, and side views were aligned orthogonally with the camera, ensuring optimal visibility for reconstruction. Additionally, the first two and last two wing beat cycles were excluded to avoid potential inconsistencies caused by takeoff or landing dynamics. The selected wing beat cycle corresponded to a phase of stable flight, with clearly visible wing deformation, providing an ideal dataset for accurate kinematic analysis. The subsequent reconstruction focused solely on the left wing, with an identical

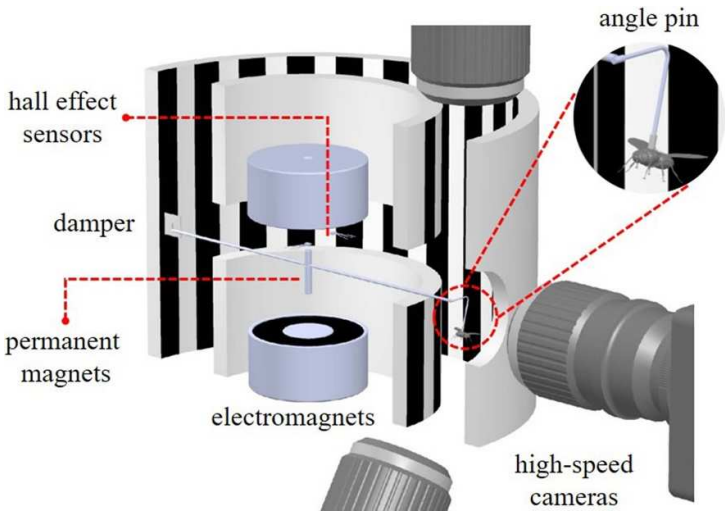

Figure 1. Experimental setup of MAGLAV Flight Mill with shaft with damper, three permanent magnets acting as pivot joint, and three cameras for high-speed video recording. The flies were recorded in circular enclosure of (50 mm × 50 mm × 50 mm) using three cameras by placing them at top, side (by cutting a circular hole on the outer wall), and bottom view [31]. Reproduced with permission from [31]. © 2025 The Company of Biologists. All rights reserved.

Table 1. Morphological parameters of the blue bottle flies (*Calliphora Vomitoria*).

Parameters	Values
Total mass, m (mg)	48.5
Wingspan length, R (mm)	8.0
Body length, bl (mm)	10.4
Chord length, c (mm)	2.25
Wing area, S_w (mm^2)	18.1
Aspect ratio, $AR = R^2/S_w$	3.50
Flapping frequency, f_w (Hz)	148
Forward flying speed, U_∞ (m s^{-1})	1.24

process applied to the right wing. Noteworthy is the absence of any distinct body deformation or rotation throughout the reconstruction process.

As depicted in figure 2(a) the real representation of the blue bottle fly is showcased, accompanied by expanded images detailing the particulars of its wing and antenna [32]. Figure 2(b), on the other hand, presents the meticulously reconstructed iteration of the blue bottle fly, encompassing both its body and wings. The complicated surface deformation of the wing was achieved through the utilization of the twist and bend handle along its surface. Critical to the reconstruction was the strategic utilization of the twist handle to govern chordwise deformation. Specifically, the leading edge within the twist handle was rendered fixed, while the manipulation of chordwise deformation along the root and spanwise deformation was steadily regulated through the establishment of distinct angles for the root and tip handle within the twist handle. This meticulous approach was adopted in consideration of the inherent structural characteristics of the blue bottle fly, where chordwise deformation predominates over spanwise deformation.

The reconstruction of wing deformation extended across a single beat cycle, summarizing 28 instants. Controls embedded within the twist handle were configured based on the underlying structure and deformations of the wing veins. Subsequently, the 3D reconstruction of the body and left wing was aligned with the natural deformation observed across 28 instances in high-speed recordings.

Accurate alignment procedures were applied to both bottom and side views in the high-speed recording, with wing deformation sequentially applied first to the side view and then to the bottom view through adept manipulation of the twist handle. The schematic representation of this process is revealed in figure 3(a), portraying both side and bottom views with the reconstructed body and wings. Further insight into the reconstruction of the wing surface and deformation from bottom and side view is provided in figures 3(b), and (c) visually conveys the precise alignment of the wings with the recording. Following the completion of the reconstruction process spanning 28 frames, Fourier interpolation was systematically employed to interpolate the unstructured surface mesh. This procedure yielded

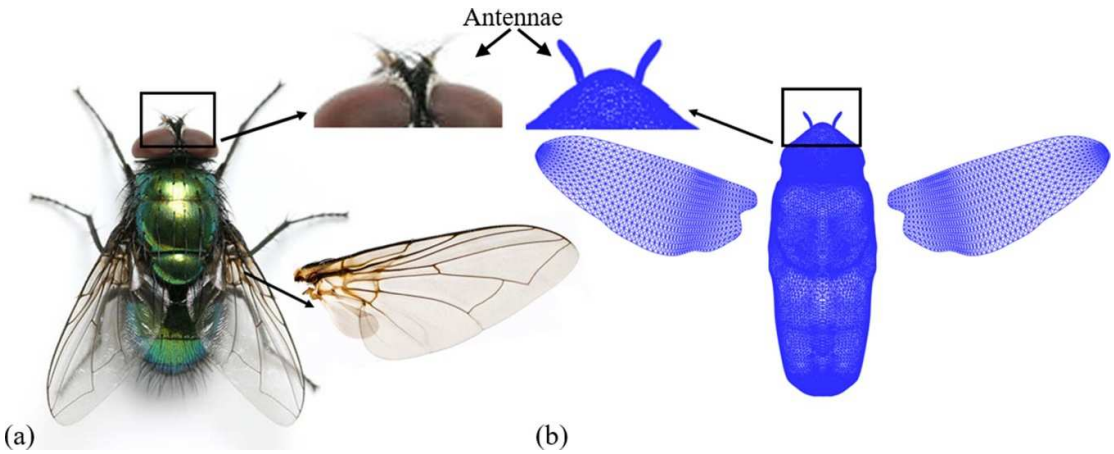

Figure 2. (a) The real blue bottle flies, with expanded antenna and wing. The blue bottle fly image is credited to the ecologic entomology under the common license [32]. (b) The computational model of the blue bottle fly with the reconstructed wing, body, and antenna. Reproduced with permission from [32].iStock.com/Antagain © 2025 iStockphoto LP.

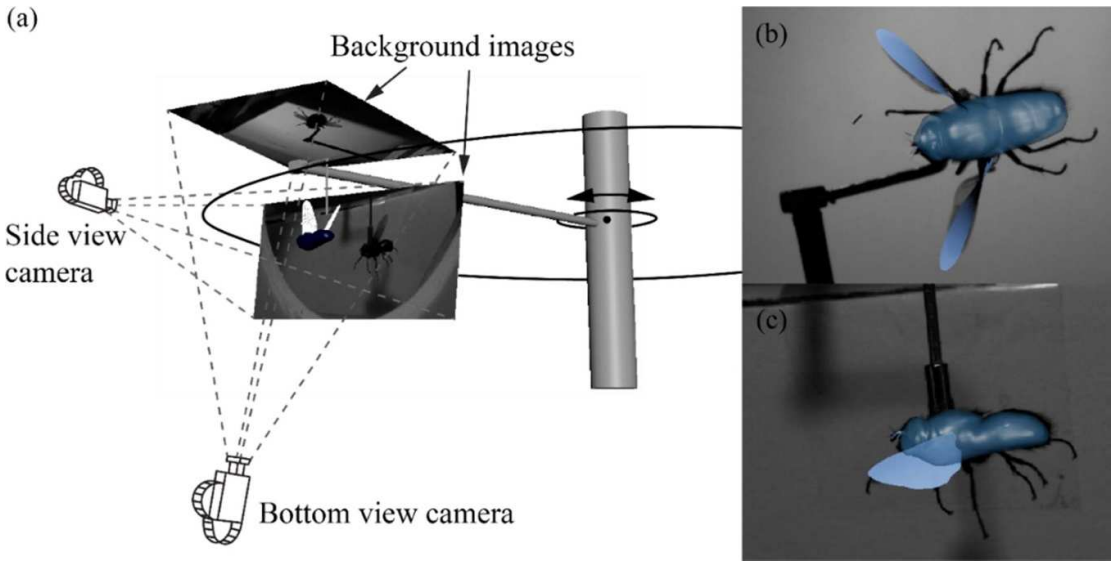

Figure 3. (a) The scaled virtual scene based on the actual filming scene with reconstructed model overlapping with the background images from side view and bottom view (b) projection of the reconstructed wings on the high-speed recording for bottom view (c) projection of the reconstructed wings on the high-speed recording for side view.

high temporal frequency data, equivalent to 960 time-steps per beating cycle, subsequently serving as input for our CFD solver. The reconstruction approach employed in this study has been successfully applied in our previous research on insect flight [6, 12, 33].

The temporal progression of wing kinematics in blue bottle flies (*Calliphora vomitoria*), along with the definition of Euler angles, is illustrated in figure 4. These Euler angles encompass the stroke angle (ϕ), pitch angle (ψ), and deviation angle (θ). Notably, the body pitch angle remains at zero during the fly's forward flight at a speed of 1.24 m s^{-1}, resulting in a seamlessly smooth forward flight. For the specified case, the wingbeat frequency and wing stroke amplitude are reported as 148 Hz and 130°, respectively. The trajectory of the wingtip follows a figure-of-eight pattern, with the deviation angle encompassing a range of 34°. Notably, the deviation angle varies from −20° to 14° for both wings. The pitch angle (ψ) is measured precisely at the midpoint of the wingspan. Over this interval, the pitching angle ranges from 40° to −69°, exhibiting an amplitude of 109°. It is important to note that the values presented align with previously reported findings for the blue bottle fly [30, 31].

Figure 4(c) present a more detailed visualization of the wing's deformation, specifically showing the wing pitching at 25%, 50%, and 75% of the wingspan. This representation clearly demonstrates the twisting of the wing along its span, with the values indicat-

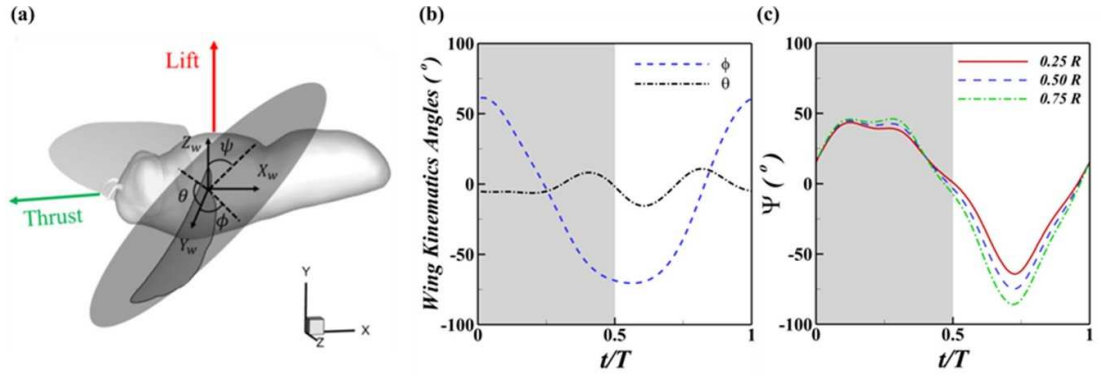

Figure 4. (a) The definition of Euler angles stroke ϕ, pitch ψ and deviation θ with lift and thrust in body fitted coordinate system. (b) The time course (t/T, where T is the time-period for one flapping cycle) of Euler angles (c) wing pitch at 25%, 50%, and 75% of the wingspan.

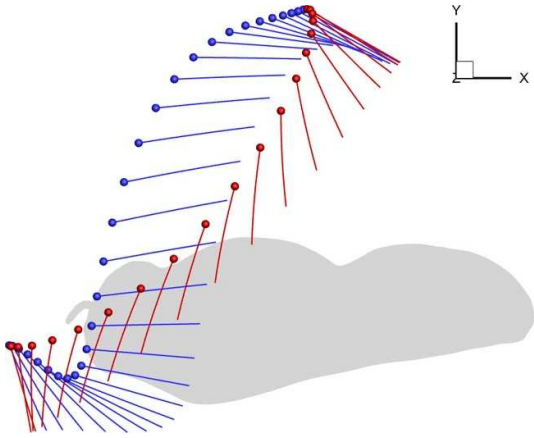

Figure 5. Wingtip trajectory with the wing chord (blue line for downstroke and red line for upstroke), dot on chord line show the leading edge.

ing a measurable twisting effect, particularly around the mid-span of the wing. This twisting effect is an essential characteristic of wing flexibility and plays a crucial role in the insect's aerodynamic performance. To complement the understanding of wing dynamics, figure 5 portrays the wing chord position. This visualization provides additional insights into the sophisticated interplay of wing movements during the flight of the blue bottle fly.

2.3. Governing equations and numerical method

This study utilizes an in-house CFD solver based on the IBM to numerically solve the 3D unsteady, viscous, incompressible Navier–Stokes equations, as described by:

$$\frac{\partial u_i}{\partial x_i} = 0,$$

$$\frac{\partial u_i}{\partial t} + \frac{\partial \left(u_i u_j\right)}{\partial x_j} = -\frac{1}{\rho}\frac{\partial p}{\partial x_i} + \nu \frac{\partial}{\partial x_j}\left(\frac{\partial u_i}{\partial x_j}\right) \quad (1)$$

where u_i ($i = 1, 2, 3$) are the velocity components in the x-, y- and z-directions, respectively; p is the pressure; ρ and ν are the fluid density and kinematic viscosity, respectively.

The numerical solution of the equations is achieved through a cell-centered collocated grid arrangement for the primitive variables (u_i and p). Temporal integration is performed using the fractional step method, ensuring stability and accuracy, while spatial discretization employs a second-order central difference scheme for precision. To address the challenge of simulating flow around the complex, moving boundaries of beating wings, an immersed-boundary-method-based approach is utilized. In this method, boundary conditions are enforced directly on the immersed boundaries using a ghost-cell procedure. This approach offers a significant advantage over traditional boundary-conforming methods by eliminating the need for complex re-meshing algorithms. Consequently, it greatly reduces the computational cost associated with simulating flows around intricate and dynamically moving boundaries, making it an efficient and robust choice for such simulations. Our immersed-boundary-method can be categorized as a discrete forcing approach wherein forcing is directly incorporated into the discretized Navier–Stokes equations. The movement of the immersed boundaries (wings and body) is prescribed according to the image-based reconstruction as described in section 2.1. This immersed-boundary-method has successfully been used to simulate insect flights [34, 35] and bio-inspired propulsions [36, 37]. Validations of the current in-house CFD solver can be found in our previous studies [33, 38–40].

The governing equation of odorant advection–diffusion in the air phase can be written as:

$$\frac{\partial C'}{\partial t} + U_i \frac{\partial C'}{\partial x_i} = D \frac{\partial^2 C'}{\partial x_i \partial x_i} \quad (2)$$

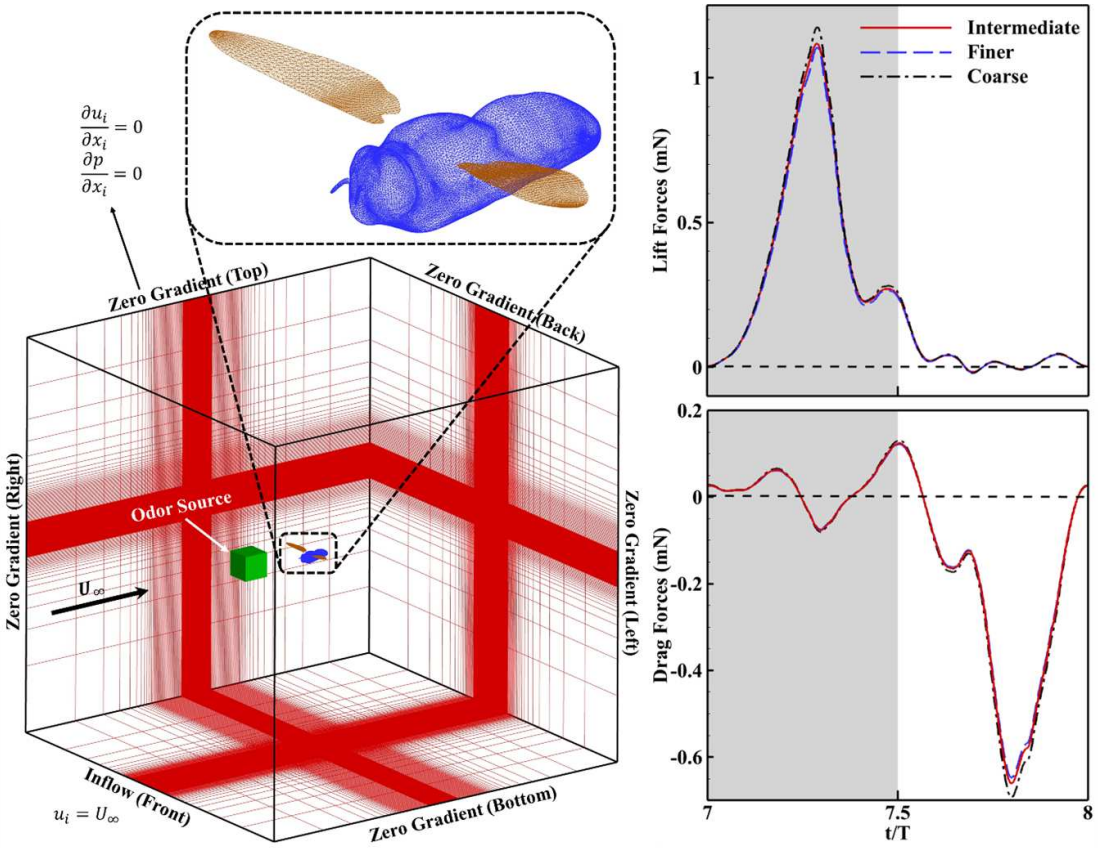

Figure 6. (a) Computational domain and mesh with the boundary condition with expanded image of fly (b) comparison of the time course of the lift and drag for the course, intermediate, and finer grid.

where i (= 1, 2 and 3) indicates the components in the x-, y- and z-directions; $C' = C/C_0$ is the normalized odor intensity and C_0 is the odor intensity of the odor source; U_i is the face-centered velocity obtained by interpolation of the cell-centered velocity u_i; D is the odor diffusivity.

At each time step, the odor advection–diffusion equation is solved using the velocity field derived from the Navier–Stokes equations to compute the odor concentration landscape. The equation is discretized using an implicit method, ensuring second-order accuracy in space. Detailed validations of this numerical approach for simulating odor transport have been thoroughly documented in our previous studies [6, 25].

2.4. Simulation setup

The cubical mesh domain (30 R), depicted in figure 6(a), was chosen for this study. The wings and body were positioned at the center of the domain. The front boundary is given a constant inflow U_∞, and the rest of the boundary conditions are zero gradient boundary conditions. The mesh was divided into three segments: coarse, intermediate, and refined layers. The fly was situated at the domain center, within the refined layer of the mesh. Beyond this refined layer, a stretched layer was applied to the mesh. The grid size for the current simulation is specified as 7.5 million (24 ×177×177). A grid-independent study was conducted, and the time course of lift and drag forces is presented in figure 6(b). The size of the coarse grid was 6.5 million (209 ×177 ×177), while the finer grid had a size of 8.5 million (273 ×161 ×193). The results indicate that there is a discrepancy of less than 2% in forces between the finer and baseline grids.

The flow field is characterized by Reynolds number (Re). In the current study, the Reynolds number is defined by $\mathrm{Re} = U_\infty R/\nu$, where U_∞ is the forward flight velocity, R is the wingspan length, and ν is the kinematic viscosity (around 1.56×10^{-5} m^2 s^{-1} for air at room temperature of 25 °C). Based on the experimental measurement (table 1), the Reynolds number is 636.

The odorant transport phenomenon is characterized by both Re and Schmidt number (Sc), which are combined as the Péclet number ($\mathrm{Pe} = \mathrm{Re} \times \mathrm{Sc}$). Here, the Péclet number is 954 which indicates a ratio between the rate of advection and the rate of diffusion. With the Péclet number in the order of 10^3, the advective odor transportation is faster than the diffusive odor transportation. Schmidt number is a ratio between kinematic viscosity and odor diffusivity ($\mathrm{Sc} = \nu/D$). The typical natural odor has

relatively low diffusivity (D) in the air at normal temperature and pressure is in an order of $10^{-5}\,\mathrm{m^2\,s^{-1}}$. In this study, the odor diffusivity D is set to $1.04\times10^{-5}\mathrm{m^2\,s^{-1}}$ which leads the Schmidt number Sc to 1.5.

During the simulations, a cubic odor source positioned $2R$ in front of the fly model, releases odorants at constant intensity C_0 starting at $(t/T=0)$.The odor intensity of the odor source is fixed at a constant value C_0. The odor intensity in this study will be normalized by C_0, denoted as C/C_0. So, for example, the normalized odor intensity C/C_0 at the odor source has constant value 1. At all boundaries of the flow domain, the boundary conditions for the advection-diffusion equation are zero gradient. The body surface and wings of the fly are set as non-slip and no-penetration boundary conditions.

2.5. Evaluation of aerodynamic performance and olfaction sensitivity

The instantaneous aerodynamic forces acting on the blue bottle fly's wings are obtained through the surface integration of pressure and shear stress over the wings and body. The lift force F_L and drag force F_D are then calculated by projecting these integrated forces onto the vertical and horizontal directions, respectively. This allows for a detailed analysis of the fly's flight mechanics, where lift is essential for maintaining altitude and drag must be minimized for efficient forward motion. Aerodynamic power P_a is the power required to overcome air resistance during flight. It is defined as the scalar product of the velocity vector and the aerodynamic force acting on the wing:

$$P_\mathrm{a}=-\iint(\Delta P+\Delta\tau)\,\boldsymbol{n}\cdot\boldsymbol{u}_c\mathrm{d}s. \tag{3}$$

Where ΔP represents the pressure difference across the wing surface,$\Delta\tau$ denotes the shear stress difference, $\boldsymbol{n}$ is the unit normal vector of the element on the wing, $\boldsymbol{u}_c$ is the cell-centered velocity vector of the triangular element on the wing, and ds is the area of the triangular element.

To determine the instantaneous odor concentration, the normalized odor intensity C/C_0 is calculated by solving the advection–diffusion equation. Considering that the blue bottle fly's primary olfactory organs are its antennae, two virtual probes are positioned along each antenna to gather time-series data of odor intensity as it passes these points. One is placed at the tip of the antenna and the other is placed at the root. The relative odor surge (δ) is defined in following equation which is used to quantify the odor fluctuation,

$$\delta=\frac{\left(\frac{C}{C_0}\right)_\mathrm{peak}-\left(\frac{C}{C_0}\right)_\mathrm{mean}}{\left(\frac{C}{C_0}\right)_\mathrm{mean}}. \tag{4}$$

For our calculations, we assume complete odor absorption when odorant-laden air encounters the antenna. This simplification is reasonable for modeling the diffusion and binding processes of chemical species through the boundary layer to olfactory receptors. By combining these assessments of aerodynamic performance and olfaction sensitivity, we can thoroughly evaluate the blue bottle fly's flight efficiency and its capability to detect environmental odors, both of which are vital for its survival and behavior.

3. Results and discussion

In this section, we present the findings of our comprehensive study on the unsteady aerodynamics and olfactory function of the blue bottle fly (*Calliphora vomitoria*). The results are organized into three subsections for clarity and detailed discussion. First, we evaluate the unsteady aerodynamics and olfactory performance of the blue bottle fly, highlighting key metrics and observations. Next, we examine the effects of wing-induced flow on olfaction, exploring how the aerodynamic environment created by wing movements influences the fly's ability to detect odors. Finally, we investigate the impact of wing flexibility on both aerodynamic and olfactory sensitivity, analyzing how structural variations in the wings affect these critical functions.

3.1. Evaluation of aerodynamic and olfactory functions of blue bottle fly

In this section, we delve into a comprehensive analysis of the aerodynamic and olfactory performance of the reconstructed blue bottle fly. Our exploration begins with an in-depth discussion of the fly's drag and lift characteristics, which are pivotal in understanding its overall aerodynamic efficiency. By examining these forces, we aim to show how the blue bottle fly maintains its flight stability and maneuverability in various environmental conditions.

Subsequently, we will explore the complex flow physics that governs the interaction between the fly's wings and the surrounding air. This section will highlight the vortex structures, airflow patterns, and pressure distributions that are crucial for generating the necessary aerodynamic forces. Understanding these flow phenomena is essential for comprehending how the blue bottle fly achieves both efficient and agile flight.

Finally, we will examine the olfactory performance of the blue bottle fly, which plays a vital role in its ability to locate food sources and navigate its environment. By investigating the sensory mechanisms and olfactory structures, we aim to shed light on how the fly's olfactory system integrates with its flight dynamics to enhance its foraging efficiency and survival.

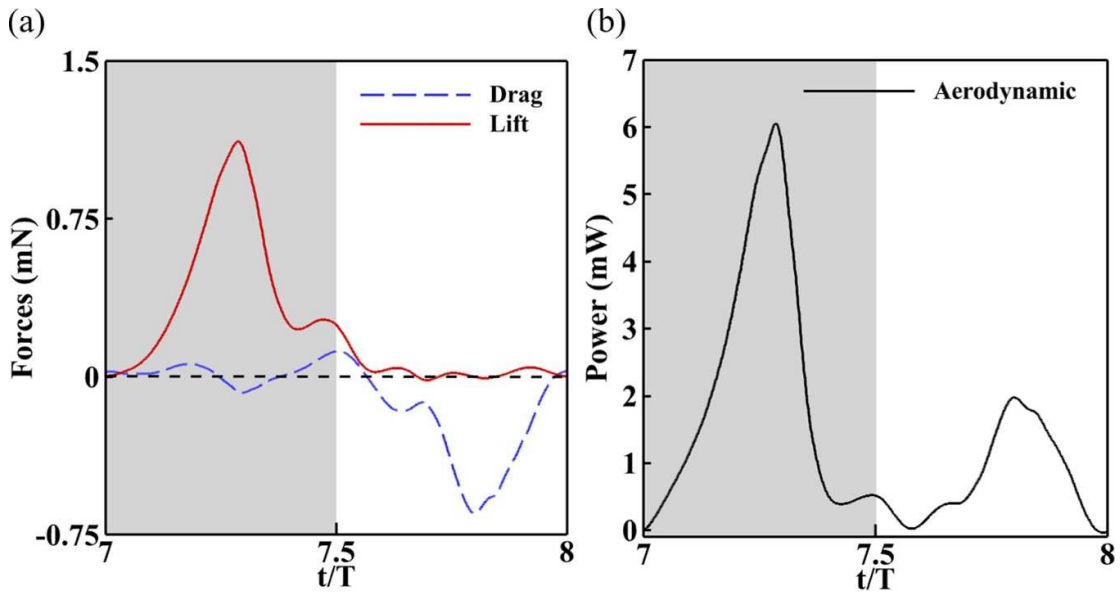

Figure 7. (a) The time history of lift F_L and drag F_D produced by a single wing and the blue bottle fly. (b) The time history of aerodynamic power P_a.

Table 2. The distribution of lift and drag forces for the blue bottle fly.

	Downstroke average	Upstroke average	Total average	Peak value
Lift (**mN**)	0.2100	0.0216	0.2316	1.2500
Drag (**mN**)	0.01833	−0.1697	−0.1514	−0.6500

3.1.1. Lift, drag and aerodynamic power

The aerodynamic performance of the reconstructed blue bottle fly is shown in figure 7. Figure 7(a) illustrates the lift and drag forces acting on the fly, while figure 7(b) presents the aerodynamic power required by the fly. The lift force is predominantly generated during the downstroke of the flapping cycle, as shown by the grey area in figure 7(a). The average lift value during the downstroke is 0.21 mN, while for the upstroke, it is 0.0216 mN as shown in table 2. The overall average lift for the complete cycle is 0.2316 mN. Conversely, the drag force is mainly produced during the upstroke. The average drag force during the downstroke is 0.01833 mN, and for the upstroke, it is −0.1697 mN. The average drag force for the entire cycle for one wing is −0.1514 mN. The peak lift value is 1.25 mN, occurring around the mid-downstroke, while the peak drag force is −0.65 mN, occurring around the mid-upstroke. The total weight of the fly is 0.47 mN (48 mg). The cumulative lift generated by both wings is 0.4632 mN, accounting for approximately 98.5% of the fly's weight. Notably, a significant portion of the thrust force is produced during the upstroke, attributable to the more horizontal motion of the wing, as demonstrated in figure 5.

The aerodynamic power utilization for flapping wings reaches its peak during both the downstroke and upstroke, with a significant decrease in power during the transition between strokes. Notably, during pronation and supination, the power value approaches zero when translational speed is zero. In our CFD simulation, the estimated power for a flexible wing is 1.51 mW. Figure 8 illustrates the average lift and power for the entire flapping cycle across the wing surface. The left wing exhibits the average lift value, while the right wing illustrates the average aerodynamic power. Analysis of figure 8 reveals that a substantial portion of the lift force is generated around the leading edge of the wing, consistent with findings from a prior study [25]. Conversely, most of the power consumption occurs around the wingtip of the wing.

3.1.2. Vortex structure

The vortices produced by the flapping motion play a crucial role in enhancing the aerodynamic performance of insect flights. Key flow characteristics, including the leading-edge Vortex (LEV), tip vortex (TV), trailing-edge vortex (TEV), and vortex loop, are observed in the current simulated flight. The vortex structure around the wings of the blue bottle fly, using the Iso-surface Q-criterion, is shown in figure 9. Four distinct time instants are selected to explain the vortex structure, as discussed below.

At the initiation of the flapping cycle (t/T= 7.125), the stroke plane angle undergoes an increase, indicating acceleration and triggering LEV

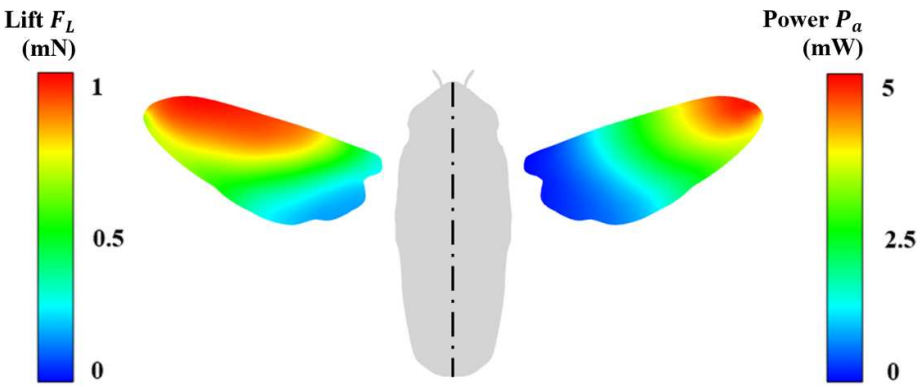

Figure 8. The distribution of cycle-averaged lift (left) and aerodynamic power consumption (right) on the wing surfaces.

production. This phenomenon is well-supported by existing literature, where the relationship between stroke plane angle and LEV generation has been extensively explored. According to prior studies [29], the acceleration during this phase promotes the development of the LEV, which is characterized by a relatively small but progressively growing vortex. The stability and attachment of the LEV to the leading edge of the wing have been identified as crucial factors contributing to enhanced lift forces during the early stages of the flapping cycle. This enhancement arises from the vorticity near the wing's leading edge, inducing beneficial changes in airflow dynamics. By the attachment of airflow to the wing's upper surface, the LEV effectively delays stall, ensuring prolonged lift generation. Moreover, the associated high-pressure region on the upper surface, created by the vorticity, contributes to an upward force, augmenting overall lift production. The pressure differential and efficient downwash effect generated by the LEV further optimizes aerodynamic efficiency, collectively resulting in increased lift forces and improved flight performance. This intricate interplay of vortical structures showcases the vital role of the LEV in shaping the aerodynamic forces essential for successful flight. The first row of figure 9 provides a visual representation through top, side, and perspective views, clearly illustrating the presence of the LEV along with visible vortices from the preceding cycle.

Post mid-downstroke (t/T= 7.375), the LEV becomes fully developed and stronger, continuing in its attachment compared to the cycle's initiation. As the wing decelerates following the mid-downstroke, it instigates the formation of a vortex loop, as shown in the second row of figure 9. The influence of these vortex loops and vortices on aerodynamic performance has undergone thorough examination in the literature [29]. The vortex loop created post mid-downstroke serves as an additional aerodynamic mechanism. Its presence influences the wing's interaction with the surrounding airflow, contributing to the generation of lift and aiding in maintaining stability during the complex flapping motion. The unsteady flow features, exemplified by the vortex loop, exemplify the adaptability of the blue bottle fly's flight strategy, showcasing how unsteady aerodynamics contribute to the overall efficiency of its aerial maneuvers.

Following supination (t/T= 7.625), wing deceleration induces the generation of TV, as shown in the third row of figure 9. The TV is a critical feature that influences the aerodynamic performance of the blue bottle fly. TV, formed at the wingtip during deceleration, introduces a rotational flow pattern that enhances the lift-to-drag ratio. This vortex structure contributes to the overall efficiency of the upstroke by optimizing the aerodynamic forces acting on the wing. The vortex shedding develops due to the upstroke motion of the wing, and concurrently, the formation of TEV occurs. The wing engages with the wake created during the downstroke, known as wing-wake interaction. The TEV further refines the wing-wake interaction, impacting the generation of thrust forces during the upstroke. The intricate interplay of these vortex structures during supination highlights the dynamic and adaptive nature of the blue bottle fly's flight strategy, optimizing aerodynamic performance throughout the entire flapping cycle. Throughout this phase of the upstroke, the wing's horizontal movement initiates thrust production, propelling the fly forward. The thrust force exhibits an increasing trend until the mid-upstroke, gradually diminishing as the upstroke concludes.

As the wing flaps upward (t/T=7.875), a stronger TEV is generated, and the wing engages with the vortex loop, as shown in figure 9. The TEV towards the end of the upstroke, its strengthened formation is integral to optimizing the wing's interaction with the surrounding airflow. The TEV further

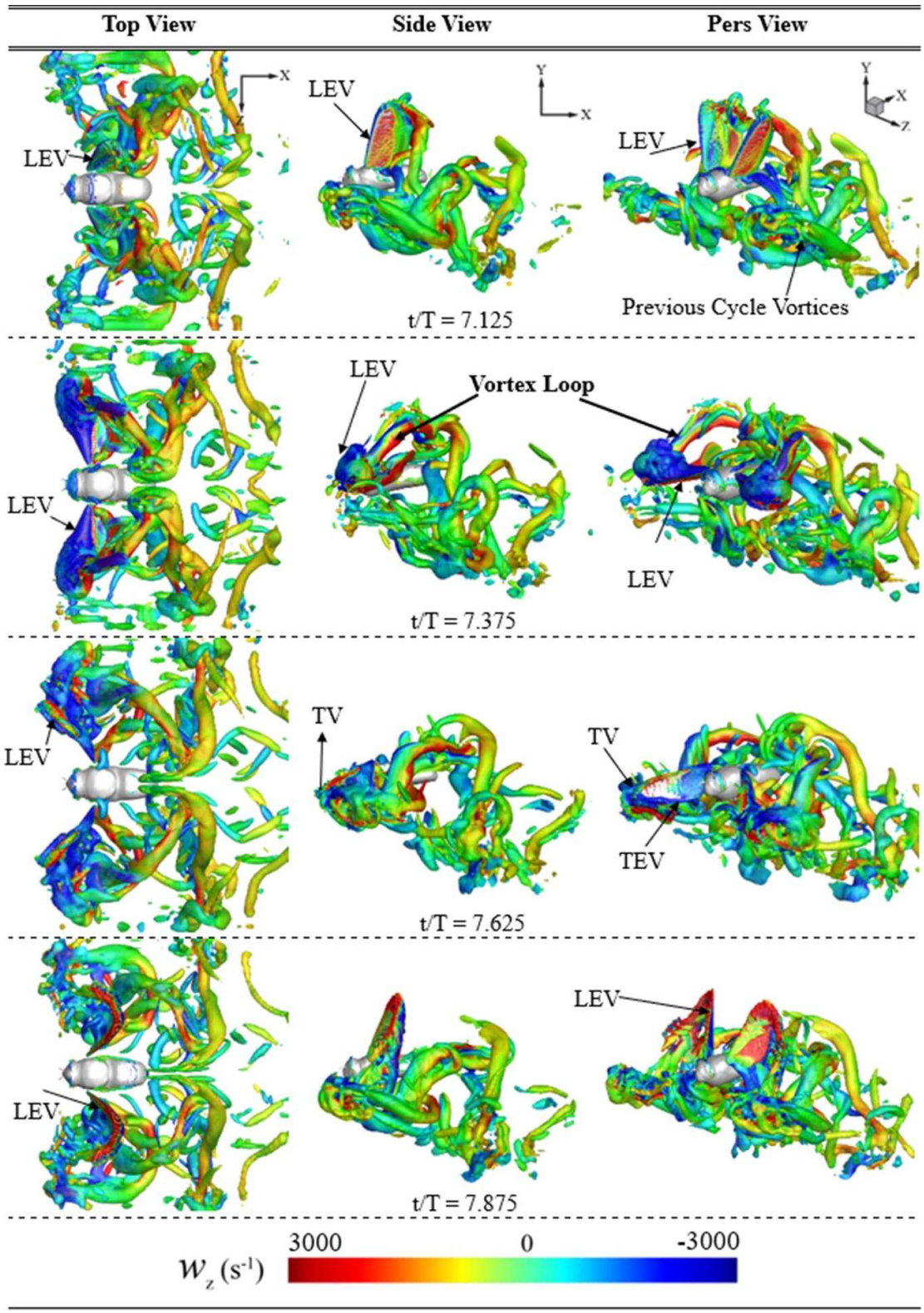

Figure 9. Vortex structure (Q-criterion) colored by the spanwise vorticity at $t/T = 7.125$, 7.375, 7.625, and 7.875.

refines the wing-wake interaction, promoting efficient thrust production during this phase. This critical phase toward the end of the upstroke involves the end of various vortex structures, including LEV from the initiation, TV during deceleration, and the intensified TEV. This synergy among the LEV, TV, and TEV highlights the complexity and adaptability of the blue bottle fly's flight strategy. By strategically utilizing various vortex structures throughout the flapping cycle, the fly maximizes thrust generation, showcasing the sophisticated aerodynamic mechanisms employed for efficient and agile flight.

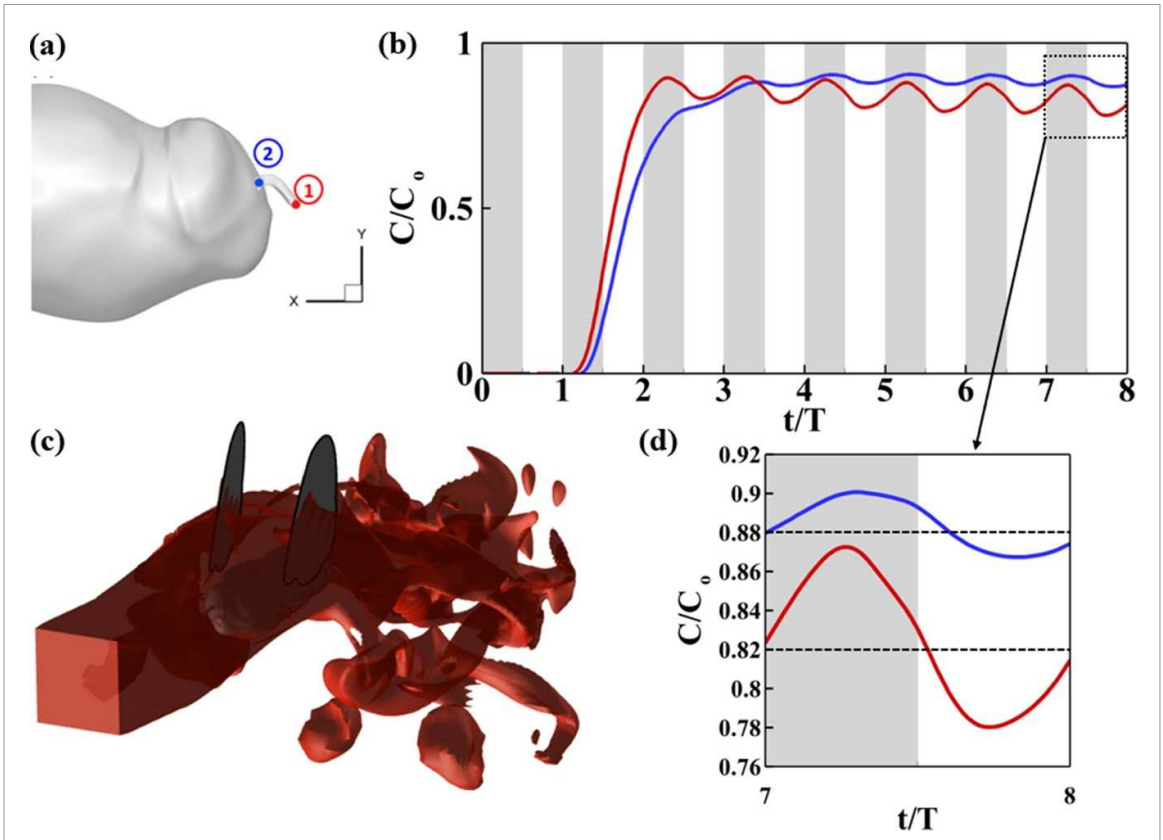

Figure 10. (a) The probe locations for measuring the odor intensity. (b) Time history of the odor intensity at the selected locations. (c) Position of the odor source in numerical simulation. (d) The odor intensity for the 8th flapping cycle.

3.1.3. Olfactory performance

To quantify the odor intensity along the bluebottle fly's antenna, we addressed the challenge by solving the advection–diffusion equation at each time step. Two specific locations along the antenna were chosen for intensity measurements. The time history of the normalized odor intensity (C/C_0) for these two probes, positioned at the tip and close to the head of the fly, is presented in figure 10(a). The reasoning behind selecting these locations was to capture the dynamic nature of odor concentration over the antenna.

Figure 10(b) illustrates the outcomes for an 8-flapping cycle, allowing for the examination of odor flow development over the antenna. It is noteworthy that, initially, the odor concentration is unstable, stabilizing after two cycles. Subsequently, the odor exhibits fluctuations synchronized with the flapping motion. As the flapping velocity increases, the odor intensity rises, peaking at the end of the upstroke before declining. Comparing the two probe positions, the data indicates that the probe at the antenna's tip exhibits more pronounced fluctuations compared to the probe near the fly's head. This discrepancy highlights the spatial variability in odor intensity along the antenna.

To visually represent the odor distribution in the fluid domain surrounding the bluebottle fly's wing and body, we generated contour plots for the odor intensity (C/C_0). Figure 10(c) depicts a numerical simulation where a uniform odor source was strategically positioned in front of the bluebottle fly. This simulation aids in comprehending the spatial dispersion of odor around the fly during its wing-flapping motion. The resulting contours provide a comprehensive illustration of how the odor intensity varies across the fluid domain, contributing valuable insights into the interaction between the bluebottle fly and its olfactory environment.

In our study, we observed that the flapping motion of the blue bottle fly generates oscillations on both probes 1 and 2. Figure 10(d) displays the odor distribution with fluctuation for the 8th flapping cycle in the baseline case. The aim is to analyze and understand how these oscillations contribute to the fly's behavior and how the wing flapping motion influences odor dispersion. These oscillations exhibit an average concentration value of 0.82, with a relative odor surge (δ), of 0.06 for the downstroke and 0.04 for the upstroke for probe 1. The average values and the time history of changes in oscillations for both the downstroke and upstroke are illustrated in table 3.

For probe 1, the average value during the downstroke is 0.854, while for the upstroke, it is 0.794. The time history reveals that during the downstroke, the

Table 3. Cycle-averaged odor intensity (Avg.) and relative odor surge (δ) for probe 1 and probe 2.

	Probe 1		Probe 2	
	Avg.	δ	Avg.	δ
Downstroke	0.854	0.073	0.890	0.023
Upstroke	0.794	0.048	0.870	0.028
Cycle	0.820	0.122	0.884	0.051

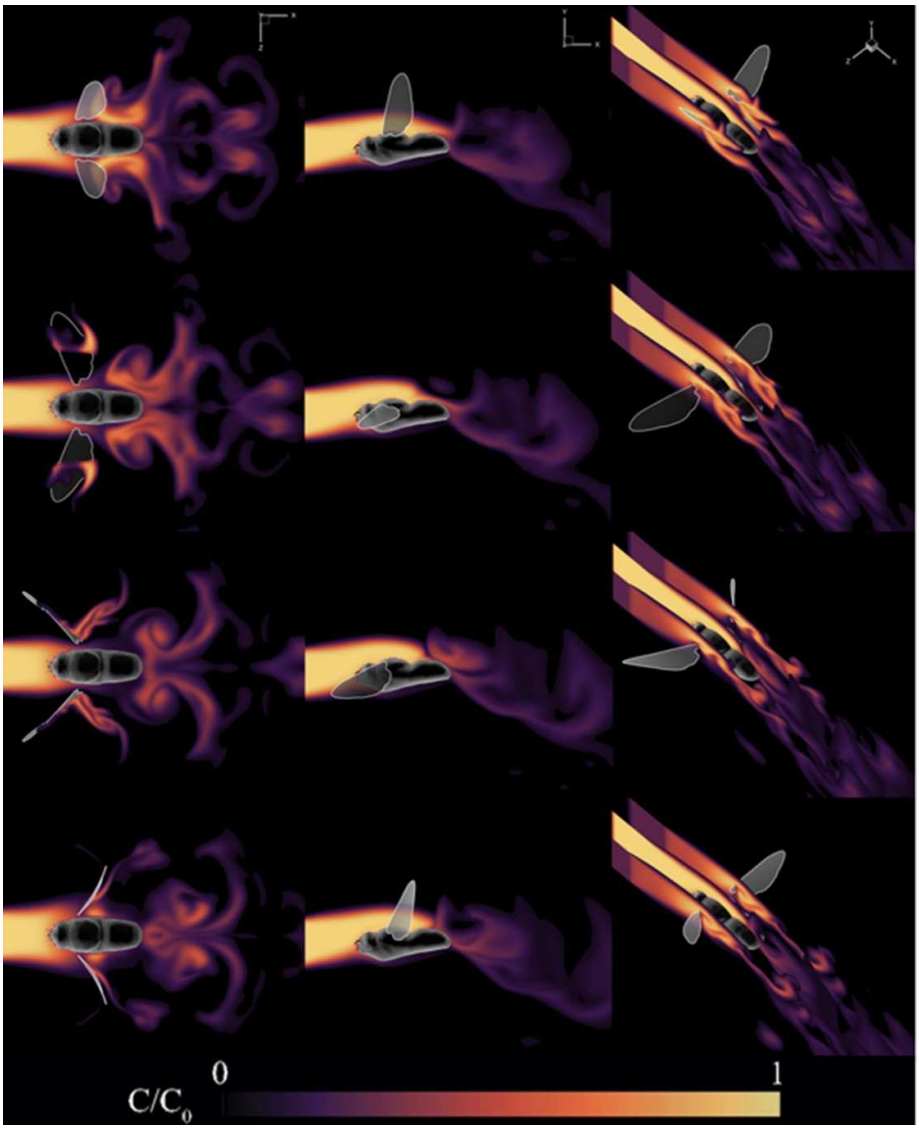

Figure 11. The contour of odor intensity C/C_0 at $t/T = 7.125$, 7.375, 7.625, and 7.875 for the top (left), side (center) and Pers (right) view.

odor concentrations for the antenna probes increase, whereas during the upstroke, it moves away from the antenna. This phenomenon is crucial because insects typically sense values greater than the average to avoid sensory fatigue.

The odor flow field is shown in figure 11, where three columns represent the top view, side view and perspective view respectively. For the top view contour, a bottom plane slice in the middle is placed whereas for the side view a lateral slice is used. In the perspective view, three different slices along the surfaces of each wing were used. With the development of the air flow, odor passes over the blue bottle fly. Because of the flapping motion of the insect's wing, the odor started fluctuating around the antenna. The results reveal that as the air flow develops, the odor traverses over the bluebottle fly, influenced by the distinctive flapping motion of its wings. During the downstroke initiation (t/T= 7.125), the wing guides the odor towards the antenna. The mid-downstroke phase (t/T= 7.375) intensifies this effect, pushing more odor towards the antenna. The

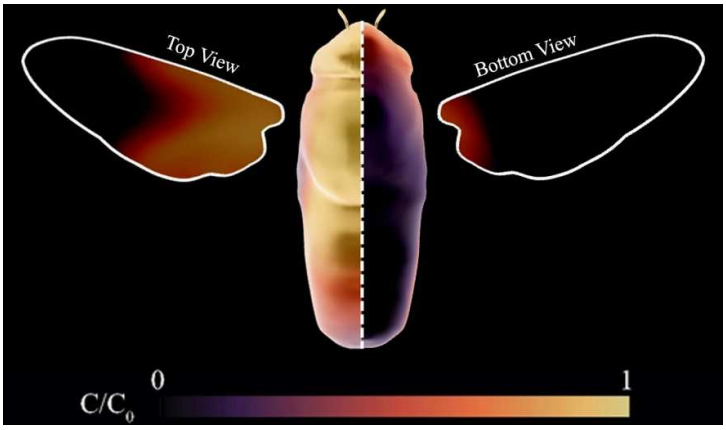

Figure 12. The distribution of cycle averaged odor intensity C/C_0 on the surface of wings and the body.

opposite trend for the upstroke can also be seen from figure 11.

The upstroke phase ($t/T = 7.625$), conversely, sees the flow moving away from the antenna as the wing retracts. The odor predominantly targets the head of the bluebottle fly. The concentration disparities observed between the probe close to the head and the one at the tip of the antenna resonate with findings in research by on odor coding in insects [25]. Their work suggests that different regions of the antennae may exhibit varied sensitivities to odor stimuli, influencing the observed fluctuations. The average odor intensity over the cycle is shown in figure 12. The right half wing shows the bottom view whereas left view shows the top view. From the figure the odor has maximum intensity at the head of the blue bottle fly. This shows the antenna is well positioned for the highly efficient odor guided flight.

3.2. Effects of wing-induced flow on olfaction

To assess the influence of the wing's flapping motion on odor distribution, we conducted simulations for a 'body-only' case and compared the odor concentration outcomes with those from the full-wing case for two deliberately positioned probes. Figure 13 presents the results, revealing important insights into the dynamics of odor concentration in the presence and absence of wing motion.

Remarkably, the 'body-only' case exhibits a consistent maximum odor concentration at both probes, registering a value of 1. Importantly, in this scenario, there is an absence of odor flux fluctuations, signifying a stable and unchanging odor field surrounding the insect's sensory appendages. This finding is consistent with previous literature highlighting the role of the body in generating and maintaining localized odor concentration around sensory organs [41–46]. In contrast, the simulation incorporating flapping wing motion introduces a dynamic and fluctuating odor flow over the antenna, as depicted in figure 13. This dynamic aspect is crucial for the insect's odor-guided navigation during flight, aligning with the observations of Jones *et al* [44] and Distel *et al* [43].

The constant odor flux observed in the 'body-only' case, without the beneficial fluctuation induced by wing motion, is known to lead to olfactory adaptation. This process results in poor olfactory performance, as highlighted by research on insect olfaction. To mitigate odor fatigue, insects experience reduced sensitivity to familiar odors over time. To overcome this, they employ various techniques to introduce odor oscillations. Claverie *et al* [41, 42] demonstrated that walking bees oscillate their antennae to effectively detect odors in strong odor fields. In a separate study, Kellar and Weissburg observed that animals exposed to short pulse plumes exhibited degraded tracking performance [45]. Levakova *et al* found that pheromone encounters are most effectively detected when the concentration follows a naturally intermittent time course [46]. These findings highlight the significance of odor oscillations in improving olfactory sensitivity and tracking performance in the presence of constant or repeated odor sources.

Our results underscore the critical role of wing-induced odor fluctuations in maintaining the sensitivity of the insect's olfactory system, ultimately contributing to more effective odor-guided navigation during flight. This dynamic interplay between wing motion and odor concentration, as evidenced in our simulations, provides valuable insights into the adaptive mechanisms employed by insects for efficient olfactory navigation. To understand the effect of wing presence on odor, figure 14 illustrates the odor concentration contour for both cases. The figure highlights the difference between upstream and downstream scenarios in both cases. In the presence of wings, the odor demonstrates oscillations, contrasting with the body-only case where the odor concentration remains constant. In the body-only case,

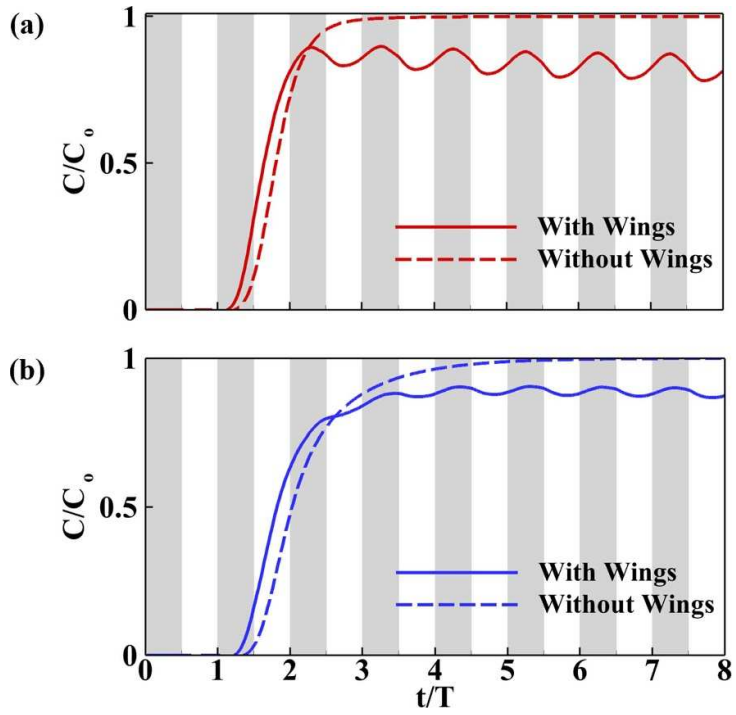

Figure 13. Comparison of odor intensity C/C_0 between the baseline case (with flapping wings) and the body-only case (W/O flapping wing) at probe 1 (a) and probe 2 (b).

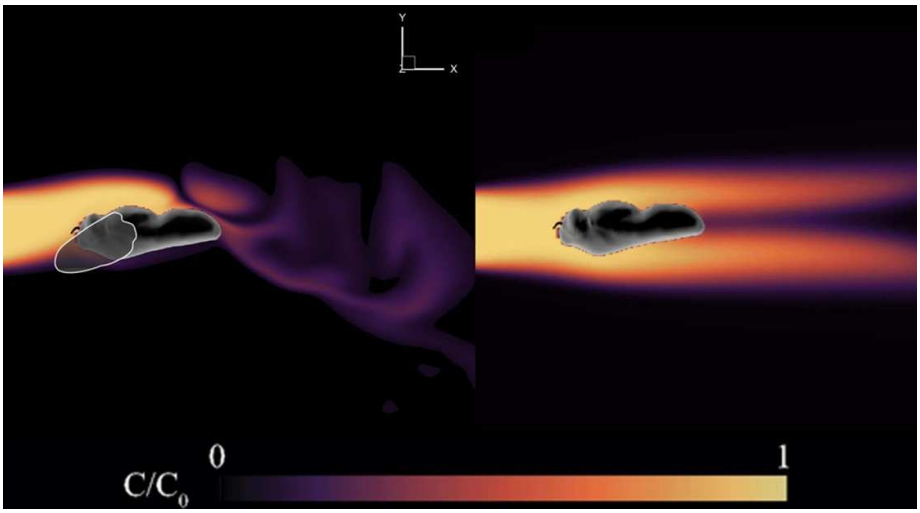

Figure 14. The lateral-center contour of odor intensity C/C_0 for the baseline case (left) and the body-only case (right).

the odor concentration is higher over the body compared to the baseline case. This observation suggests that the primary advantage of the insect's flapping motion lies in generating fluctuations in odor concentrations around the antenna. Insects leverage this phenomenon to navigate efficiently in highly complex odor environments.

The comparison between the baseline (with flapping wings) and body-only (without flapping wings) cases highlight the critical role of wing-induced odor fluctuations. In the body-only case, the odor concentration remains constant and leads to olfactory adaptation, resulting in poorer olfactory performance. In contrast, the baseline case with flapping wings introduces beneficial fluctuations that prevent sensory fatigue and enhance odor-guided navigation. This finding aligns with previous research on insect olfaction, emphasizing the importance of dynamic odor flux for maintaining sensitivity and effective odor tracking.

3.3. Effects of wing flexibility on aerodynamic and olfactory performance

Time courses of lift and drag forces are depicted in figure 15. Both rigid and flexible wings generate lift during the downstroke and drag force during the

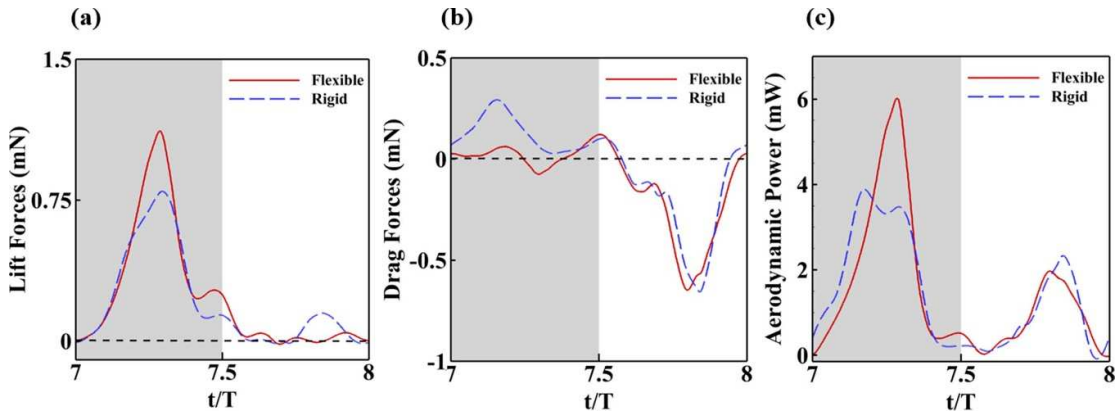

Figure 15. (a) The time history of lift F_L (b) the time history and drag F_D (c) the time history of lift P_a produced by a flexible and rigid wing of the blue bottle fly.

Table 4. Comparison of aerodynamic performance between rigid wing and flexible wing.

	Lift total (**mN**)	Drag total (**mN**)	Lift peak (**mN**)	Drag peak (**mN**)
Rigid	0.2033	−0.1251	0.82	−0.67
Flexible	0.2316	−0.1510	1.25	−0.65

upstroke. Although both types of wings exhibit similar trends in lift force, the flexible wing demonstrates higher lift force compared to the rigid wing as shown in table 4. The average lift force generated by the flexible wing is 0.2316 mN, compared to 0.2033 mN for the rigid wing, representing a 14% increase. The peak lift force for the flexible wing is 1.25 mN, whereas for the rigid wing, it is 0.82 mN. Several factors contribute to the observed difference in lift forces. The inherent flexibility of the flexible wing allows for a more adaptive response to aerodynamic forces, resulting in enhanced lift production. The flexibility of the wing might enable it to better adjust to varying airflows, leading to increased lift coefficients during the downstroke.

On the other hand, the rigid wing, being less adaptable, experience lesser lift performance due to its limited ability to respond to dynamic changes in the surrounding airflow. The overall trend of lift force for both cases is nearly the same, but during the upstroke, the lift force produced by the rigid wing surpasses that of the flexible wing. Further investigation is required to understand the specific aerodynamic mechanisms influencing this observed shift in lift forces during the upstroke.

The comparison o vortex structures between the rigid and flexible wings at mid-downstroke, as illustrated in figure 16, reveals that the LEV in the flexible wing is stronger than that of the rigid wing. This strengthened LEV enhances the suction effect on the wing surface, leading to a higher lift output in the flexible wing case. The increased vorticity suggests that wing flexibility plays a crucial role in stabilizing and strengthening the LEV, which in turn improves aerodynamic performance. These findings highlight the aerodynamic advantage of wing flexibility, demonstrating how insects may exploit structural compliance to optimize force production and maneuverability during flight.

The impact of wing flexibility on olfactory performance represents a relatively underexplored area of research. In this section, we delve into the effects of wing deformation on the olfactory performance of the blue bottle fly, as illustrated in Figure. The time history of two probes, one for rigid wings and another for flexible wings, is plotted to elucidate these effects.

A comparison of intensity between rigid and flexible wings is detailed in table 5. For probe 1, the flexible wing exhibits fluctuations with a higher concentration compared to the rigid wing. Although the oscillation amplitude for both cases at probe 1 is nearly identical, the concentration normalized by the reference concentration (C/C_0) is lower for the rigid wing than the flexible wing. This suggests that, while the amplitude of oscillation is similar, the flexible wing leads to a more pronounced impact on the odor concentration.

Similarly, for probe 2, the trend is alike to that of probe 1, but with a reduced fluctuating amplitude. The odor concentration field for both rigid and flexible wings is visually represented in figure 17. While the overall odor field for both cases appears similar, the intensity level for the rigid wing is notably lower compared to the flexible wing. These findings suggest that wing flexibility may play a crucial role in enhancing the olfactory performance of insects,

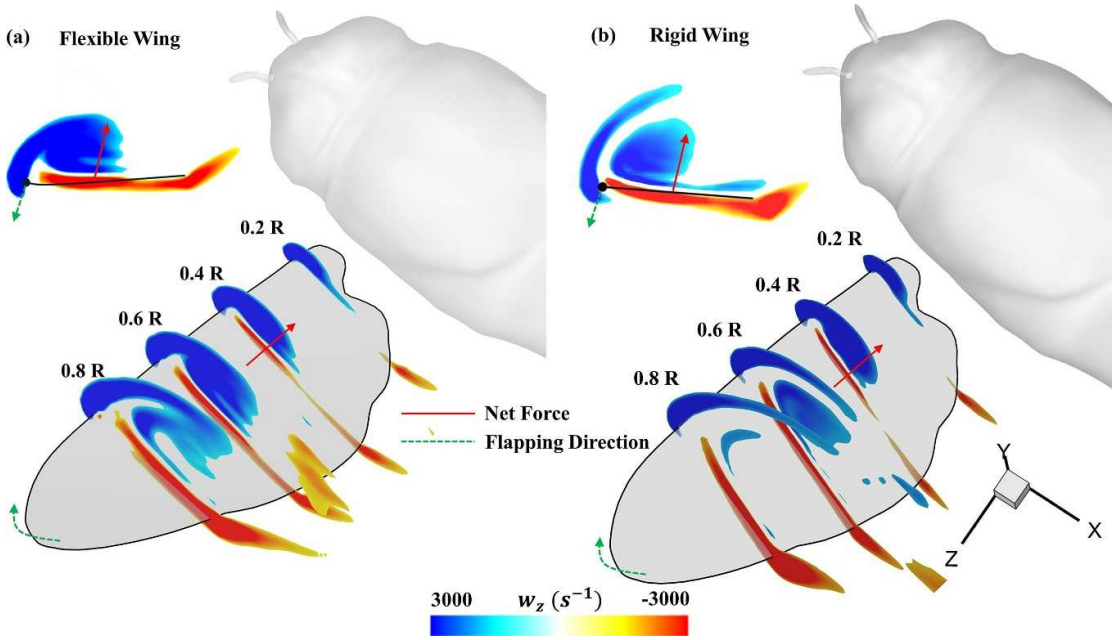

Figure 16. Vortex comparison of the flexible wing (a) and rigid wing (b).

Table 5. Cycle-averaged odor intensity (Avg.) and relative odor surge ($\langle\delta\rangle$) for the rigid and flexible wings.

		Flexible		Rigid	
		Avg.	δ	Avg.	δ
Probe 1	Downstroke	0.854	0.073	0.672	0.077
	Upstroke	0.794	0.048	0.614	0.065
	Cycle	0.820	0.122	0.644	0.142
Probe 2	Downstroke	0.890	0.023	0.710	0.028
	Upstroke	0.870	0.028	0.658	0.024
	Cycle	0.884	0.051	0.698	0.052

influencing both the concentration levels and oscillation patterns of odor cues. Further research is essential to comprehensively understand the intricate relationship between wing flexibility and olfactory capabilities in insects.

Notably, the relative odor surge (δ) for both wing types remains nearly consistent, measuring 0.073 and 0.077 for downstroke and 0.048 and 0.065 for upstroke for probe 1, while for probe 2, it is 0.023 and 0.028 for downstroke and 0.028 and 0.024 for upstroke. However, a significant distinction arises in the average odor concentration values, with the rigid wing exhibiting lower values (0.644 for probe 1 and 0.698 for probe 2) compared to the flexible wing (0.820 for probe 1 and 0.884 for probe 2). This result highlights the impact of wing flexibility on odor dispersion dynamics. The flexible wing enhances the mean intensity of odor signals (up to 25%), providing a more effective olfactory performance for the insect. The adaptability of flexible wings allows for better modulation of odor plumes, facilitating improved detection and interpretation of olfactory cues, ultimately contributing to superior olfactory performance compared to rigid wings. Figure 18 shows the lateral-center contour of odor intensity C/C_0 for the baseline (left) and the rigid wing case (right).

In summary, flexible wings outperform rigid wings in both aerodynamic and olfactory functions. Flexible wings generate higher lift forces, with an average of 0.2316 mN compared to 0.2033 mN for rigid wings—a 14% increase. This enhanced lift production is attributed to their ability to adapt to varying aerodynamic forces and respond dynamically to changes in airflow. During the downstroke, flexible wings achieve higher lift coefficients, while rigid wings, constrained by their inflexibility, exhibit lower lift performance.

In terms of olfactory function, flexible wings also demonstrate superior performance. Time histories of odor intensity near probes around flexible wings reveal higher concentrations than those around rigid wings. This indicates that flexible wings enhance the

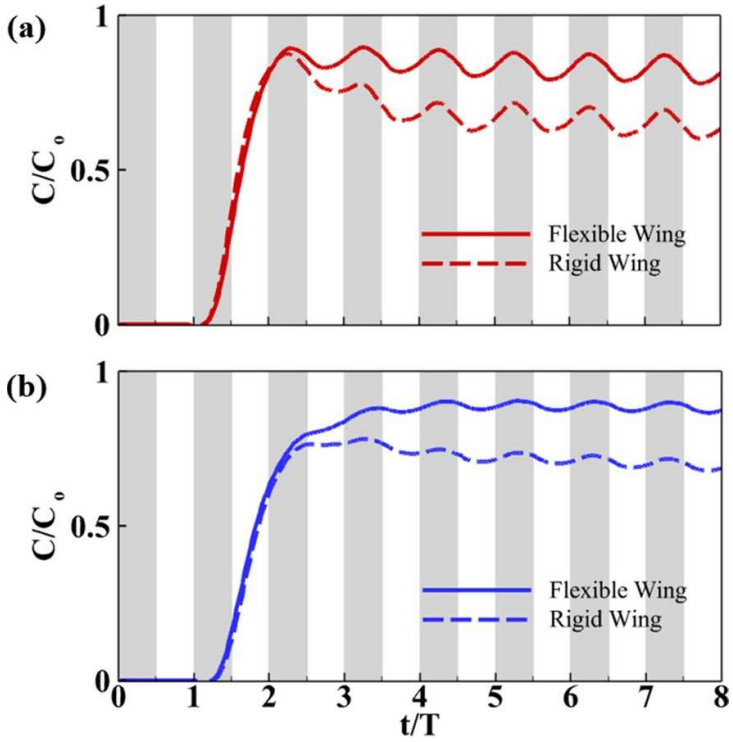

Figure 17. Comparison of odor intensity C/C_0 between the flexible and the rigid wing at probe 1 (a) and probe 2 (b).

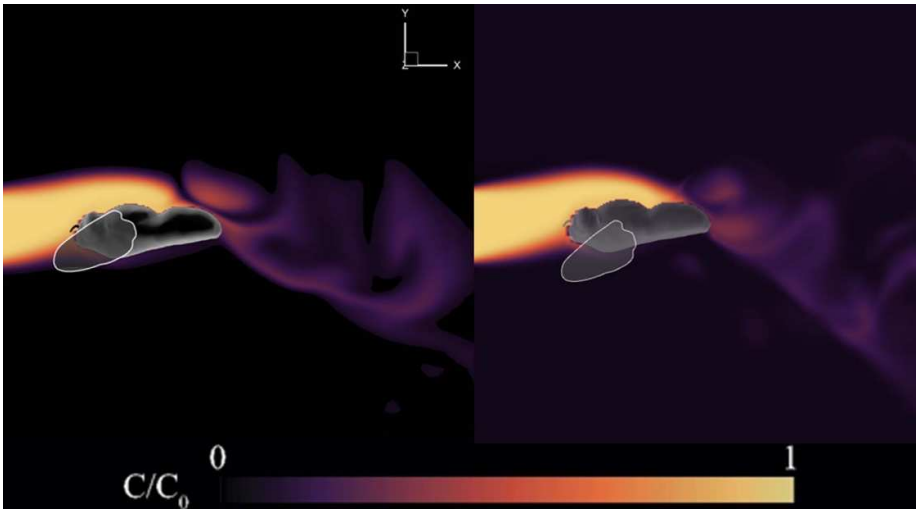

Figure 18. The lateral-center contour of odor intensity C/C_0 for the baseline (left) and the rigid wing case (right).

modulation of odor plumes, improving the insect's ability to detect and interpret olfactory cues. The dynamic interaction between wing motion and odor concentration observed in simulations highlights the critical role of wing flexibility in maintaining effective olfactory navigation during flight.

4. Conclusions

Insects, especially flies, rely on wind-borne odor plumes for critical behaviors such as locating food, identifying mates, and evading predators. Our research illuminates the intricate interplay between flapping wings, unsteady aerodynamics, and olfactory capabilities in flying insects, with a particular focus on the blue bottle fly. Through CFD simulations, we demonstrated that flapping wing kinematics generate odorant fluctuations, accounting for 12.2% of the odor intensity magnitude. This enhances the fly's olfactory function and helps mitigate odorant fatigue. Compared to a rigid wing, a flexible wing not only increases aerodynamic force by 14% but also amplifies the mean magnitude of odor intensity reaching the fly's antennae by 25%. Our findings

enrich the understanding of insect flight and olfaction, addressing a significant gap in knowledge about how the deliberate manipulation of flow fields supports sensory functions. This study highlights the potential for further investigation into the intentional modulation of flow fields for sensory purposes across diverse insect behaviors. Ultimately, our research advances the understanding of the sophisticated mechanisms employed by flying insects to navigate their environments and underscores the broader implications of flow-field modulation in odor-guided navigation.

Data availability statement

All data that support the findings of this study are included within the article (and any supplementary files).

Acknowledgment

The simulation work is supported by National Science Foundation (CBET-2453175) and Airforce Office of Scientific Research (FA9550-24-1-0122) to C. Li. The experimental work and related analyses are funded by National Science Foundation (CMMI 1554429) and Airforce Office of Scientific Research (FA9550-23-1-0705) to B. Cheng.

ORCID iDs

Naeem Haider https://orcid.org/0009-0002-5228-7130
Zhipeng Lou https://orcid.org/0009-0008-0421-9313
Shih-Jung Hsu https://orcid.org/0009-0003-2095-1532
Bo Cheng https://orcid.org/0000-0002-6982-0811
Chengyu Li https://orcid.org/0000-0002-8379-2423

References

[1] Knaden M and Graham P 2016 The sensory ecology of ant navigation: from natural environments to neural mechanisms *Annu. Rev. Entomol.* **61** 63–76
[2] Taylor G K and Krapp H G 2007 Sensory systems and flight stability: what do insects measure and why? *Adv. Insect Physiol.* **34** 231–316
[3] Li C, Dong H and Zhao K 2018 A balance between aerodynamic and olfactory performance during flight in Drosophila *Nat. Commun.* **9** 3215
[4] Talley J L, White E B and Willis M A 2023 A comparison of odor plume-tracking behavior of walking and flying insects in different turbulent environments *J. Exp. Biol.* **226** jeb244254
[5] Cardé R T and Willis M A 2008 Navigational strategies used by insects to find distant, wind-borne sources of odor *J. Chem. Ecol.* **34** 854–66
[6] Lou Z, Lei M, Dong H and Li C 2024 Wing–antenna interaction reduces odour fatigue in butterfly odour-tracking flight *J. Fluid Mech.* **998** A45
[7] Fuller S B, Straw A D, Peek M Y, Murray R M and Dickinson M H 2014 Flying Drosophila stabilize their vision-based velocity controller by sensing wind with their antennae *Proc. Natl Acad. Sci.* **111** E1182–E91
[8] Willis M A, Avondet J L and Zheng E 2011 The role of vision in odor-plume tracking by walking and flying insects *J. Exp. Biol.* **214** 4121–32
[9] Shyy W, Kang C-K, Chirarattananon P, Ravi S and Liu H 2016 Aerodynamics, sensing and control of insect-scale flapping-wing flight *Proc. R. Soc.* A **472** 20150712
[10] Haider N, Shahzad A, Qadri M N M and Shams T A 2021 Aerodynamic analysis of hummingbird-like hovering flight *Bioinsp. Biomim.* **16** 066018
[11] Haider N, Shahzad A, Mumtaz Qadri M N and Ali Shah S I 2021 Recent progress in flapping wings for micro aerial vehicle applications *Proc. Inst. Mech. Eng.* C **235** 245–64
[12] Lionetti S, Hedrick T L and Li C 2022 Aerodynamic explanation of flight speed limits in hawkmoth-like flapping-wing insects *Phys. Rev. Fluids* **7** 093104
[13] Dong H, Bode-Oke A T and Li C 2018 *Learning From Nature: Unsteady Flow Physics In Bioinspired Flapping Flight* (InTech Rijeka)
[14] Patel M, Kulkarni N, Lei H H, Lai K, Nematova O, Wei K and Lei H 2022 Experimental and theoretical probe on mechano-and chemosensory integration in the insect antennal lobe *Front. Physiol.* **13** 1004124
[15] Houot B, Burkland R, Tripathy S and Daly K C 2014 Antennal lobe representations are optimized when olfactory stimuli are periodically structured to simulate natural wing beat effects *Front. Cell Neurosci.* **8** 159
[16] Gaudry Q, Nagel K I and Wilson R I 2012 Smelling on the fly: sensory cues and strategies for olfactory navigation in Drosophila *Curr. Opin. Neurobiol.* **22** 216–22
[17] Schultheiss P, Wystrach A, Lihoreau M and Schwarz S 2020 Insect navigation *Encyclopedia of animal cognition and behavior* eds J Vonk and T Shackelford pp 1–8
[18] Tripathy S, Staudacher E M, Peters O, Kalwar F, Hatfield M and Daly K 2010 Odors pulsed at wing beat frequencies are tracked by primary olfactory networks and enhance odor detection *Front. Cell. Neurosci.* **4** 1133
[19] Willis M A, Ford E and Avondet J 2013 Odor tracking flight of male Manduca sexta moths along plumes of different cross-sectional area *J. Comp. Physiol.* A **199** 1015–36
[20] Shigaki S, Ando N, Sakurai T and Kurabayashi D 2023 Analysis of odor tracking performance of silk moth using a sensory-motor intervention system *Integr. Comp. Biol.* **63** 343–55
[21] Liberzon A, Harrington K, Daniel N, Gurka R, Harari A and Zilman G 2018 Moth-inspired navigation algorithm in a turbulent odor plume from a pulsating source *PLoS One* **13** e0198422
[22] Menzel R and Greggers U 2013 Guidance by odors in honeybee navigation *J. Comp. Physiol.* A **199** 867–73
[23] Saxena N, Natesan D and Sane S P 2018 Odor source localization in complex visual environments by fruit flies *J. Exp. Biol.* **221** jeb172023
[24] Freas C A and Spetch M L 2023 Varieties of visual navigation in insects *Animal Cogn.* **26** 319–42
[25] Lei M, Willis M A, Schmidt B E and Li C 2023 Numerical investigation of odor-guided navigation in flying insects: impact of turbulence, wingbeat-induced flow, and schmidt number on odor plume structures *Biomimetics* **8** 593
[26] Lei M and Li C 2023 Wings and whiffs: understanding the role of aerodynamics in odor-guided flapping flight *Phys. Fluids* **35**
[27] Lei M and Li C 2020 Numerical investigation of the passive pitching mechanism in odor-tracking flights *AIAA Aviation 2020 Forum* 3016
[28] Lionetti S, Hedrick T L and Li C 2023 Numerical investigation of olfactory performance in upwind surging hawkmoth flight *AIAA AVIATION 2023 Forum* 4242
[29] Engels T, Wehmann H-N and Lehmann F-O 2020 Three-dimensional wing structure attenuates aerodynamic

efficiency in flapping fly wings *J. R. Soc. Interface* **17** 20190804
[30] Hsu S-J and Cheng B 2020 Retinal slip compensation of pitch-constrained blue bottle flies flying in a flight mill *J. Exp. Biol.* **223** jeb210104
[31] Hsu S-J, Thakur N and Cheng B 2019 Speed control and force-vectoring of bluebottle flies in a magnetically levitated flight mill *J. Exp. Biol.* **222** jeb187211
[32] Antagain Fly Stock Photo (iStock by Getty Images) (available at: www.istockphoto.com/photo/fly-gm182898513-14070394?clarity=false)
[33] Li C and Dong H 2017 Wing kinematics measurement and aerodynamics of a dragonfly in turning flight *Bioinsp. Biomim.* **12** 026001
[34] Lei M and Li C 2020 The aerodynamic performance of passive wing pitch in hovering flight *Phys. Fluids* **32** 051902
[35] Li C 2021 Effects of wing pitch kinematics on both aerodynamic and olfactory functions in an upwind surge *Proc. Inst. Mech. Eng. C* **235** 296–307
[36] Li C and Dong H 2016 Three-dimensional wake topology and propulsive performance of low-aspect-ratio pitching-rolling plates *Phys. Fluids* **28** 071901
[37] Li C, Dong H and Cheng B 2020 Tip vortices formation and evolution of rotating wings at low Reynolds numbers *Phys. Fluids* **32** 021905
[38] Li C, Dong H and Liu G 2015 Effects of a dynamic trailing-edge flap on the aerodynamic performance and flow structures in hovering flight *J. Fluid Struct.* **58** 49–65
[39] Li C, Jiang J, Dong H and Zhao K 2017 Computational modeling and validation of human nasal airflow under various breathing conditions *J. Biomech.* **64** 59–68
[40] Lionetti S, Lou Z, Herrera-Amaya A, Byron M L and Li C 2023 A new propulsion enhancement mechanism in metachronal rowing at intermediate Reynolds numbers *J. Fluid Mech.* **974** A45
[41] Claverie N, Buvat P and Casas J 2023 Active sensing in bees through antennal movements is independent of odor molecule *Integr. Comp. Biol.* **63** 315–31
[42] Claverie N, Steinmann T, Bandjee M J, Buvat P and Casas J 2022 Oscillations for active sensing in olfaction: bioinspiration from insect antennal movements *Bioinsp. Biomim.* **17** 055004
[43] Distel H *et al* 1999 Perception of everyday odors—correlation between intensity, familiarity and strength of hedonic judgement *Chem. Senses* **24** 191–9
[44] Jones C B, Mange A, Granata L, Johnson B, Hienz R D and Davis C M 2019 Short and long-term changes in social odor recognition and plasma cytokine levels following oxygen (16O) ion radiation exposure *Int. J. Mol. Sci.* **20** 339
[45] Keller T A and Weissburg M J 2004 Effects of odor flux and pulse rate on chemosensory tracking in turbulent odor plumes by the blue crab, *Callinectes sapidus Biol. Bull.* **207** 44–55
[46] Levakova M, Kostal L, Monsempès C, Jacob V and Lucas P 2018 Moth olfactory receptor neurons adjust their encoding efficiency to temporal statistics of pheromone fluctuations *PLOS Comput. Biol.* **14** e1006586